

See discussions, stats, and author profiles for this publication at: <https://www.researchgate.net/publication/231628435>

Rings and Hexagons Made of Nanocrystals: A Marangoni Effect

ARTICLE *in* THE JOURNAL OF PHYSICAL CHEMISTRY B · NOVEMBER 2000

Impact Factor: 3.3 · DOI: 10.1021/jp002605n

CITATIONS

153

READS

56

4 AUTHORS, INCLUDING:



Mathieu Maillard

University of Lyon

23 PUBLICATIONS 1,226 CITATIONS

SEE PROFILE



L. Motte

Université Paris 13 Nord

97 PUBLICATIONS 1,881 CITATIONS

SEE PROFILE

Rings and Hexagons Made of Nanocrystals: A Marangoni Effect

M. Maillard, L. Motte, A. T. Ngo, and M. P. Pileni*

Laboratoire SRSI, Université P. et M. Curie 4, Place Jussieu, BP 52, 75252 Paris Cedex 05, France

Received: July 22, 2000; In Final Form: September 4, 2000

By controlling solvent evaporation rates, it has been possible to form micrometer rings and hexagonal arrays made of nanocrystals of different sizes, shapes and materials. Such patterns are driven by surface tension gradients that induce Bénard–Marangoni instabilities in the liquid films. The resulting self-assembled structures are consistent with theoretical prediction of hydrodynamic instabilities.

1. Introduction

Recently, several papers report the formation of large rings made of nanocrystals. They were observed with silver and barium ferrite nanocrystals. Formation of such rings was explained either in terms of wetting properties¹ or magnetic interactions.²

Self-assemblies of nanocrystals in a hexagonal compact network (2D) and in “pseudo” crystalline phases (3D) have been developed in the past few years.³ In a previous paper,⁴ we demonstrated that wetting properties, capillary forces, particle–particle, and particle–substrate interactions play a role in the self-organization of nanocrystals deposited on a substrate. Such assemblies exhibit collective properties. These are observed with silver,^{5,6} cobalt,^{7,8} and ferrite nanocrystals⁹ and are attributed to dipole–dipole interactions between nanocrystals fixed at a given distance from each other and characterized by a given size. From this, it is clear that understanding the fundamental mechanisms driving the assembly of particles at a micrometer scale brings new strategies for fabrication of well-ordered arrays of micron-sized objects.

Various phenomena are related to the Marangoni effect, such as crystal growth, paint film drying, wetting processes, and more generally thin films physics.^{10,11} In this paper, unusual patterns are reported: nanocrystals form rings and hexagonal arrays in the micrometer range. These phenomena are related to the Bénard–Marangoni instabilities of deposited liquid films.

2. Marangoni Effect

2.1. General Presentation. The primary experiments, conducted by Bénard at the end of the 19th century,¹² led to the observation of convective flows in a liquid film with hexagonal patterns. Block and Pearson^{13,14} theoretically described these experiments as surface tension induced convection. This was the beginning of many further developments in fluid mechanics, and it is still a well-studied problem because of its links with various topics and applications.^{10,11}

A brief description of the Marangoni effect that leads to formation of characteristic hexagonal pattern and hole nucleation in a fluid film is presented. Due to evaporation, a film of volatile solvent deposited on a substrate is subjected to a temperature variation between the substrate and the free surface. If this variation is large, the fluid cannot conduct enough heat and a temperature gradient is created across the film. This interface

is not perfectly homogeneous, and an infinitesimal disturbance will generate (some) “hot” and “cool” regions. The interfacial tension (γ) increases with decreasing temperature as $B = -d\gamma/dT > 0$.

These local gradients generate low and high interfacial tension areas, respectively. The surface energy ($E = \gamma S$) is minimized by decreasing the high interfacial tension areas, i.e., the cold ones. Fluid is then pulled along the surface, from the warmer to the cooler places, and consequently moves downward because it cannot be accumulated in the same place. Simultaneously, liquid moves upward to the warmer place to replace the missing liquid. Hence, the hot place is fed by warm liquid from below, which amplifies the initial disturbance, and there is convective flow through the liquid film (Figure 1). A stationary state of such a process is characterized by hexagonal patterns of convection, those observed in Bénard experiments. This fluctuation enhancement is suppressed by thermal diffusivity (κ) and the dynamic viscosity (ν) of the liquid. These two parameters decrease the convection by reducing the interfacial instabilities.

Conversely, temperature variation (ΔT), increasing thickness of the liquid film (h) and variation of the interfacial tension (B) promote this phenomenon. This is summarized by the dimensionless Marangoni number established by Pearson:¹⁴

$$M_a = (B\Delta Th)/(\rho\nu\kappa) \quad (1)$$

where ρ is the liquid density.

It must be noted that below a critical value of the Marangoni number, M_c , instabilities do not appear. Above M_c , various patterns can be obtained, depending on initial conditions.^{15,16} The critical value is determined analytically by using an additional dimensionless term $L = qh/k_{th}$ where q and k_{th} are the variation with temperature of the rate of heat loss from the free surface and thermal conductivity coefficient, respectively. This is expressed by unit area.

Two behaviors can be observed. (i) For L equal or close to zero, the system is called “isolated”. The rate of heat loss is not locally modified by a temperature perturbation at the interface. For $L = 0$, the critical value for the Marangoni number is found to be $M_c = 80$. (ii) For L far from zero, the system is called “conductive”. The rate of heat loss is greatly modified by the temperature perturbation and the surface-tension effect is reduced. An increase in L induces an increase in M_c , i.e., a higher value of M_a is needed to induce instabilities.

Far from its critical value, the Marangoni number is related to the periodicity α of the convection by¹⁴ $M_a = 8\alpha^2$, where α

* To whom correspondence should be addressed.

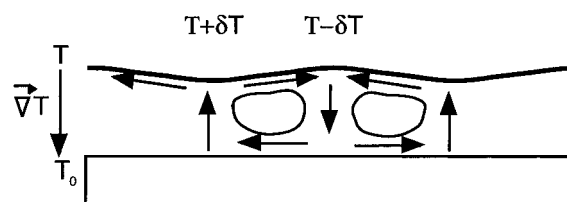


Figure 1. Schematic of the Marangoni effect.

is dimensionless. The characteristic instability wavelength is given by

$$\lambda = 2\pi h/\alpha \quad (2)$$

A number of different behaviors can be pointed out. The presence of surfactant in the liquid phase (or change in the relative amount of two solvents) induces the appearance of a concentration gradient during the evaporation process. This results in behavior similar to that of the temperature variation, ΔT .¹⁷ Similar behavior can be observed with nanocrystals instead of surfactants. When the liquid film is thick enough, the gravitational field also plays a role and generates Rayleigh buoyancy-driven convection.¹⁸ If the liquid film is very thin and/or the interface tension is very low, it is denoted as long wavelength Marangoni instabilities.^{10,19} This appears when the film thickness is in the same range as the convection. This generates long-range deformation of the surface that can lead to the film rupture by a hole nucleation process. It is especially relevant for drying of thin films such as those studied in the present paper. For very thin films (at the nanometer scale), a disjunction pressure term, due to the attractive interactions between the solid–liquid and liquid–gas interfaces, leads to a wetting transition of the thin film, inducing a hole nucleation process.²⁰

3. Experimental Section

3.1. Products. Sodium di(2-ethylhexyl) sulfosuccinate Na(AOT) and sodium borohydride were from Sigma, Isooctane, hexane, decane, and pyridine from Fluka. Hydrazine and 1-dodecanethiol were from Prolabo and Janssen chemicals, respectively. Dimethylamine and H_2S gas were from Merck, lauric acid and sodium citrate from Aldrich. The materials were not purified any further.

Various functionalized surfactants were used, as in a previously described procedure:²¹ silver di(2-ethylhexyl) sulfosuccinate Ag(AOT), cobalt, copper, and cadmium di(2-ethylhexyl) sulfosuccinate $Co(AOT)_2$, $Cu(AOT)_2$, and $Cd(AOT)_2$. The synthesis of iron(II) dodecyl sulfate $Fe(DS)_2$ is described in ref 22.

3.2. Apparatus. Electron micrographs were obtained with a JEOL electron microscope (100CX). The TEM copper grid diameter is 2 mm and it is divided in 100 μm squares. A 400 Å carbon film obtained by evaporation covers the whole grid. Optical micrographs were obtained with a Nacet NS-400.

3.3. Particle Fabrication. Nanocrystals are fabricated by using either reverse (water in oil droplets) or normal (oil in water droplets) micelles,²³ and functionalized surfactants are used. By mixing two micellar solutions containing each of the reactants during the exchange process, chemical reduction or coprecipitation takes place. By using normal micelle solutions, the chemical reaction occurs at the micelle interface between the oil core and the aqueous medium. Ferrite²⁴, silver²⁵, copper^{26,27}, cobalt⁷, cadmium sulfide²⁸, and silver sulfide³ nanocrystals are produced. Details of the syntheses are given in Appendix 1. At the end of the synthesis, nanocrystals are coated either with

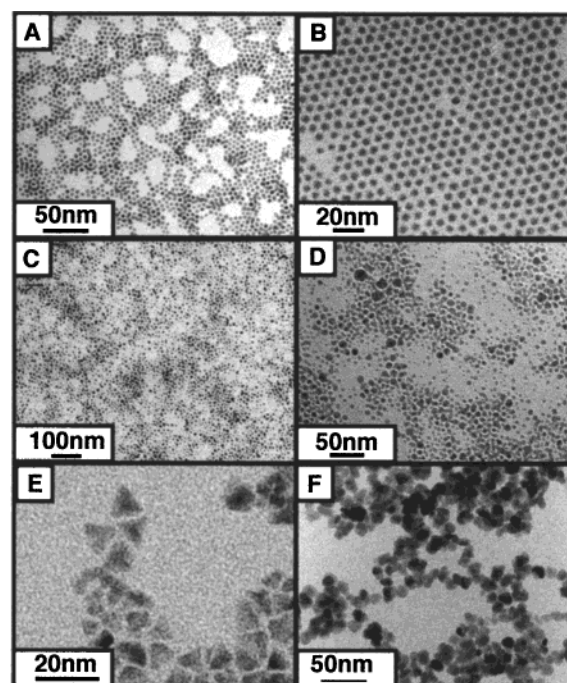


Figure 2. Silver (A), silver sulfide (B) cobalt (C), copper (D), cadmium sulfide (E), and ferrite (F) nanocrystals observed by TEM.

TABLE 1: Nanoparticle Size and Polydispersity

particles	diameter (nm)	polydispersity (%)
CdS	10 (size length)	
Ag ₂ S	5.8	14
Ag	4.4	13
Cu	6.2	40
Co	5.1	35
citrate coated γFe_2O_3	10.7	25
lauric acid coated γFe_2O_3	9.4	28

alkyl chains or citrate ions. They are then dispersed either in a nonpolar solvent or in aqueous solution. Isotropic solutions are obtained.

3.4. Sample Preparation. In previous experiments the TEM patterns showed nanocrystals either randomly dispersed or self-organized in a hexagonal network. To obtain such patterns, a drop of solution was deposited on a TEM carbon grid with a filter paper underneath. The solution migrates from the grid to the filter paper and, after a few seconds, the solvent is totally evaporated. Figure 2 shows the nanocrystals deposited on a TEM grid. As already observed, nanocrystals having a narrow size distribution self-organize into compact hexagonal networks for silver and silver sulfide particles (Figure 2A and 2B). Conversely, when the size distribution is rather wide (Table 1), nanocrystals are randomly dispersed, as observed for cobalt, copper, cadmium sulfide, and ferrite nanocrystals (Figures 2C, 2D, 2F). Under these experimental conditions the nanocrystal concentration deposited on the TEM grid was not controlled.

In the present experiments, the nanocrystal concentration is expressed by the dimensionless coverage ratio, i.e., by the ratio of the particle surface to the substrate area. This dimensionless value is more relevant than the absolute nanoparticle concentration because of the different nanoparticle sizes and densities. Experiments have been done with various nanocrystal concentrations. For a coverage ratio lower than 0.5, the solution is called “diluted”. A coverage ratio of 1 to 3 corresponds to a “concentrated” solution.

Two procedures are used. In procedure I, the nanocrystals are dispersed in a solvent and a 4- μl droplet is deposited on a

TABLE 2: P Parameters Required for the Dimensionless Marangoni Number^a

solvent	t	j	ΔT	B	h	η	κ
hexane	30	0.17	29	$9.6 \cdot 10^{-5}$	<1	$4.7 \cdot 10^{-7}$	$8.2 \cdot 10^{-8}$
“saturated” hexane	180	0.028	4.8	$9.6 \cdot 10^{-5}$	<1	$4.7 \cdot 10^{-7}$	$8.2 \cdot 10^{-8}$
water	1800	0.016	1.4	$1.5 \cdot 10^{-4}$	<1	$9 \cdot 10^{-7}$	$1.5 \cdot 10^{-7}$
decane	2700	0.001	0.4	$7.4 \cdot 10^{-5}$	<1	$1.3 \cdot 10^{-6}$	$8.2 \cdot 10^{-8}$

^a Evaporation time t (s); mass flow j (mol m⁻² s⁻¹); temperature gradient ΔT (K); surface tension variation B (J m⁻² K⁻¹); film thickness h (mm); dynamic viscosity ν (m² s⁻¹); and thermal diffusivity κ (m² s⁻¹).

TABLE 3: Numerical Estimation of the Marangoni Number and Wavelength Instability

solvent	t	j	M_a	λ
hexane	30	0.17	10^5	40 μ m
“saturated” hexane	180	0.028	1.8×10^4	90 μ m
water	1800	0.016	1571	0.4 mm
decane	2700	0.001	368	0.9 mm

TEM grid, maintained with an antcapillary tweezer. The droplet remains on its support until the solvent is totally evaporated (solvent cannot escape from the grid). In procedure II a 20- μ L droplet of “concentrated” silver particles dispersed in hexane is deposited on a glass slide and observed with an optical microscope. Under these experimental conditions, the coverage rate is large and fixed at 5.

4. Determination of the Parameters in Relation to the Marangoni Effect

According to Bénard–Marangoni theory, two parameters are needed: the Marangoni number and the characteristic instability wavelength λ (see above). The Marangoni number is $M_a = (B\Delta T h)/(\rho \nu \kappa)$. Various parameters are needed for its determination. (i) The thermal diffusivity $\kappa = k_{th} M_w / C_p \rho 10^3$, in m² s⁻¹, where k_{th} is the thermal conductivity coefficient (J s⁻¹ m⁻¹ K⁻¹), C_p the heat capacity at constant pressure (J K⁻¹ mol⁻¹), and M_w the molecular weight (g mol⁻¹). (ii) Dynamic viscosity ν (m² s⁻¹) is given by $\nu = \eta/\rho$, where η is the static viscosity. (iii) The surface tension variations with temperature, B , are given in ref 29. (iv) The temperature gradient is evaluated using the equation: $\partial T/\partial h = j \Delta H_v / k_{th}$. It is assumed that the latent heat (ΔH_v) is totally transferred to the liquid film during the evaporation process. The mass flow, j , is measured using the equation $j = n/(St)$, where n is the amount of matter which takes a time t to evaporate, deposited on a surface S . Assuming a layer height $h = 10^{-3}$ m, we obtain a temperature variation ΔT .

This evaluation of the temperature gradient is far from an ideal case. In fact, liquid film height and the temperature variation decrease during this process. For these reasons, the calculated values provide a qualitative but not quantitative description of the phenomenon.

From the Marangoni number, the characteristic instability wavelength λ is calculated (eq 2). These various parameters are given in Tables 2 and 3. Because of the uncertainty in the temperature gradient evaluation, the Marangoni number (M_a) and the instability wavelength (λ) are qualitative estimations. However, the relative variations are still relevant. Table 3 shows a large decrease in the Marangoni number with decreasing the evaporation rate (j). Hence, a much higher value of M_a is obtained for hexane in open air, compared to the others, indicating that the system is far from equilibrium. Conversely, the instability wavelength (λ) increases with decreasing the evaporation rate (j) and the variations of M_a and λ indicate a

decrease in the instabilities with decreasing this rate. At a very low evaporation rate, it is assumed that the system is close to equilibrium, without any instability.

Under our experimental conditions, liquids are volatile. This corresponds to a conducting case (L large). In fact, the flow, related to the evaporation process, markedly depends on the solvent temperature at the liquid film surface. Hence when the surface is perturbed by some temperature fluctuation, the heat transfer is locally modified. The heat transfer from “hot” places increases, inducing a decrease in the fluctuations. Hence, this phenomenon (conducting case), decreases the temperature fluctuations and consequently the thermocapillary effect. This diminishes the convection process described above.

At large L values, the Marangoni number needs to be large to reach the instability regime. This is due to an increase in the critical value, M_c , of the Marangoni number. Using decane as solvent, the Marangoni number is large compared to the critical value expected in the isolated case ($L = 0$, $M_c = 80$). This can be explained by the fact that it is a conducting case (large L values). The critical Marangoni number is then expected to be larger than that of the isolated case. Furthermore, we have to keep in mind that the Marangoni numbers given in Table 3 are not exact values (due to the uncertainty in the temperature gradient). To a first approximation, it can be assumed that by increasing the evaporation time, the system progressively reaches equilibrium.

To compare the Rayleigh buoyancy-driven and the Marangoni surface tension-driven convection, the ratio (V_R/V_M) between the Rayleigh and Marangoni convection flow speed is required. This makes it possible to determine which of them is predominant, and this is evaluated by using the approximation of $V_M \approx B\Delta T\eta$ and $V_R \approx \beta\rho\Delta Tgh^2/\eta$ given by Manneville³⁰ where $\beta = \rho^{-1}\partial\rho/\partial T$ is the coefficient of thermal expansion of the liquid and g the gravitational acceleration. With hexane solvent in open air, $V_R/V_M = \beta g \rho h^2 / B = 8 \times 10^{-3} \ll 1$. This low value indicates that the buoyancy-driven Rayleigh conduction hypothesis can be neglected.

Hence, from values given in Table 3, it is concluded that evaporation of hexane solvent in open air induces a nonequilibrium state from a thick liquid film to the final evaporation. This generates convective flows. In the presence of nanocrystals solubilized in the solvent, the evaporation process also induces a concentration gradient. The convection flows lead to variations in the local particle density.

5. Results and Discussion

Ferrite nanocrystals are coated either with lauric acid or citrate ions (see Appendix 1). Their average particle size remains the same. Depending on their coating, they are dispersed either in a non polar solvent or in aqueous solution. Procedure I is used.

Ferrite nanocrystals dispersed in hexane are deposited under air. The evaporation takes about 30 s, and the resulting rings made of nanocrystals are shown in Figure 3A. When decane (Figure 4A) or aqueous solution (Figure 4B) replaces hexane, no rings are formed and the nanocrystals are randomly dispersed. Hence, by changing the solvent used to disperse nanocrystals, rings are formed with hexane and not with other solvents. The major difference is the evaporation time of the solution. In fact, under air, it takes 30 s, 45 min, and 30 min with hexane, decane and water, respectively. Such a change in the nanocrystal organization, from rings to a random dispersion, can be attributed to the evaporation rate. All of these systems are in a nonequilibrium regime (evaporation under air). To confirm such a claim, nanocrystals dispersed in hexane were deposited on a TEM grid under a “quasi” saturated atmosphere. The evapora-

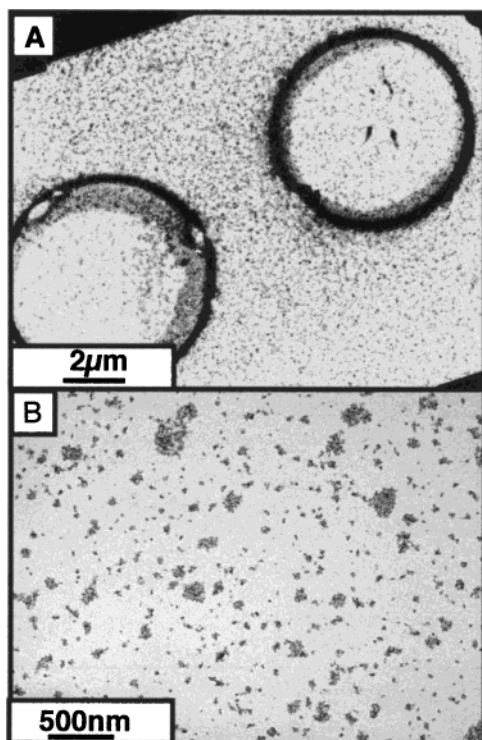


Figure 3. Ferrite nanocrystals dispersed in hexane and deposited on a TEM grid, following procedure I: (A) under air (B) under a confined atmosphere. Coverage ratio is 0.5.

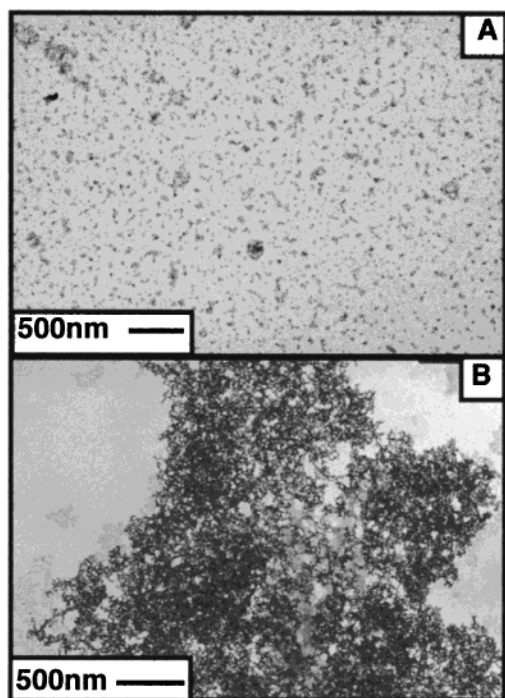


Figure 4. Ferrite nanocrystals dispersed in decane (A) and in water (B) deposited under air (procedure I). Coverage ratio is 0.5.

tion time (3 min) increases compared to that under air (30 s). Nanocrystals are then randomly dispersed (Figure 3B) without any ring formation.

From these data, it is concluded that rings made of nanocrystals are related to the evaporation rate. This is strongly confirmed by the calculated values of ΔT and M_a . The decrease in the evaporation rate induces a decrease in the temperature gradient and Marangoni number. This induces a decrease in the instabilities. By reducing the evaporation time, the system

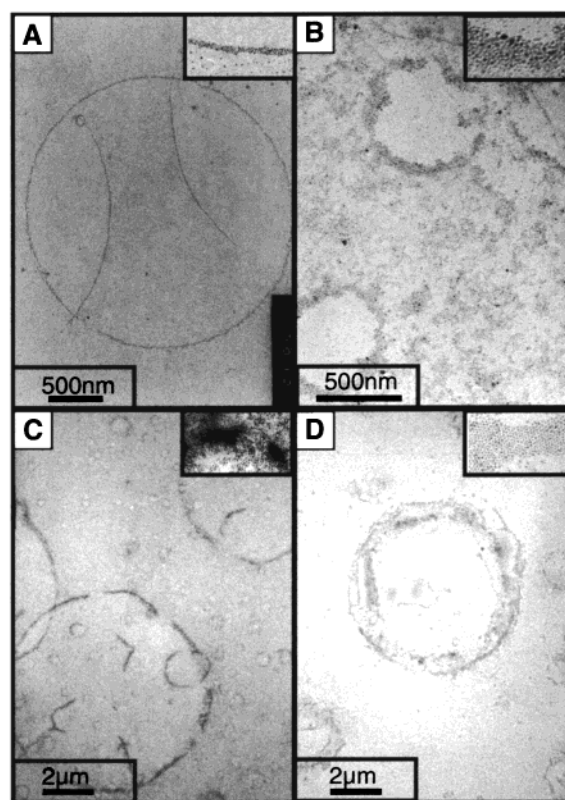


Figure 5. Nanoparticles ring obtained with a "diluted" solution of silver (A), copper (B), cobalt (C), and silver sulfide (D) observed by TEM. Coverage ratio is 0.5.

equilibrates faster than the heat loss by the evaporation process. Under such conditions, instabilities disappear and nanocrystals are randomly distributed on the carbon film. This means that formation of rings is related to the instabilities, induced by a fast evaporation process. Furthermore, it is not due to a dewetting-induced hole nucleation process of a thin film in a local equilibrium state, because these structures do not appear when the system reaches equilibrium.

At this point, an obvious question arises: is the formation of rings related to the material used (ferrite, metal, semiconductors etc.)? To answer this question, procedure I, as described above, was used for various spherical nanomaterials dispersed in hexane and evaporated under air. Rings are formed with silver (Figure 5A), copper (Figure 5B), cobalt (Figure 5C), and silver sulfide (Figure 5D). This clearly indicates that the physical properties of the nanomaterials used are not related to ring formation. Table 1 shows that the average size of particles and their size distribution markedly differ. Figure 5 clearly shows that the formation of rings is related to neither the average size nor their size distribution. However, the nanocrystals, characterized by a narrow size distribution, form rings made of nanocrystals self-assembled in hexagonal networks (insets Figure 5A and 5D). Conversely, rings are formed by nanocrystals randomly dispersed when their size distribution is rather wide (insets Figure 5B and Figure 5C). This can be related to Figure 2 where it is clearly shown that silver (Figure 2A) and silver sulfide (Figure 2B) are arranged in hexagonal networks, whereas cobalt (Figure 2C) and copper (Figure 2D) are not. It can thus be concluded that rings formed with nanocrystals having a narrow size distribution have a well-defined structure (compact hexagonal network). Conversely, when the size distribution of nanocrystals is rather wide, the rings consist of randomly dispersed particles.

Hence, deposition of nanocrystals by using procedure I, under air, induces formation of rings. This is obtained for various

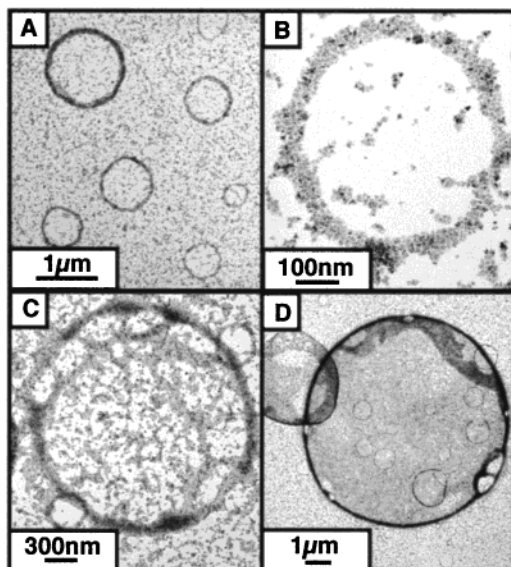


Figure 6. Various CdS rings obtained for the same sample with a “diluted” solution. Coverage ratio is 0.5.

compositions of the nanocrystals. This excludes, as already claimed,² the possibility that magnetic dipolar interactions play a role in the ring formation.

Another question arises. Does the nanocrystal shape play a role? By using procedure I, as described above (nanocrystals dispersed in hexane and solution evaporated under air), flat triangular and well crystallized CdS nanoparticles are deposited (Figure 2E). Figures 6A and 6B show that rings are also formed with triangular CdS nanocrystals. This clearly indicates that the nanocrystal shape does not play a role in the ring formation.

For any nanocrystal used, the size distribution of the rings and their annular width is narrow. The coverage ratio is lower inside than outside the rings. Features other than those described above are observed. Figure 5A shows intersecting holes whereas some trapped holes are either inside the larger one (Figure 6D) or inside the annular width (Figure 6C). Such behaviors are observed for various nanomaterials. This can be explained by the fact that during the deposition, solvent spreads on both sides of the TEM grid. Because, gravitational force does not play any role in these thin liquid films, similar phenomena occur on both sides. Both sides of the TEM grid are visualized without distinguishing one from the other. Hence these particular pictures are the superposition of the two opposite images of the carbon film. We do not have an obvious explanation for the last picture.

On increasing particle concentration and keeping procedure I, more complex organizations made of close-packed structures are observed on the TEM grid. Arrays of hexagonal patterns (Figures 7A and 7B) and/or chaotic pictures (Figures 7C) are seen. The dark “walls” correspond to nanocrystal aggregates, whereas the bright regions correspond to low particle density areas. This is again obtained, whatever the nature of nanocrystals. These structural changes are due to the increase in nanocrystal concentration because it is the only parameter that has been modified. These patterns are similar in shape to those observed in Bénard’s experiment with liquid films and attributed to a Marangoni effect. This is consistent with theories where a concentration gradient induces an increase in the Marangoni number and consequently an increase in instabilities, such as that observed for a temperature gradient.

A “concentrated” solution of silver nanocrystals is deposited on a glass slide (This surface is chosen because it is more convenient for a wetting study at a macroscopic scale.) This

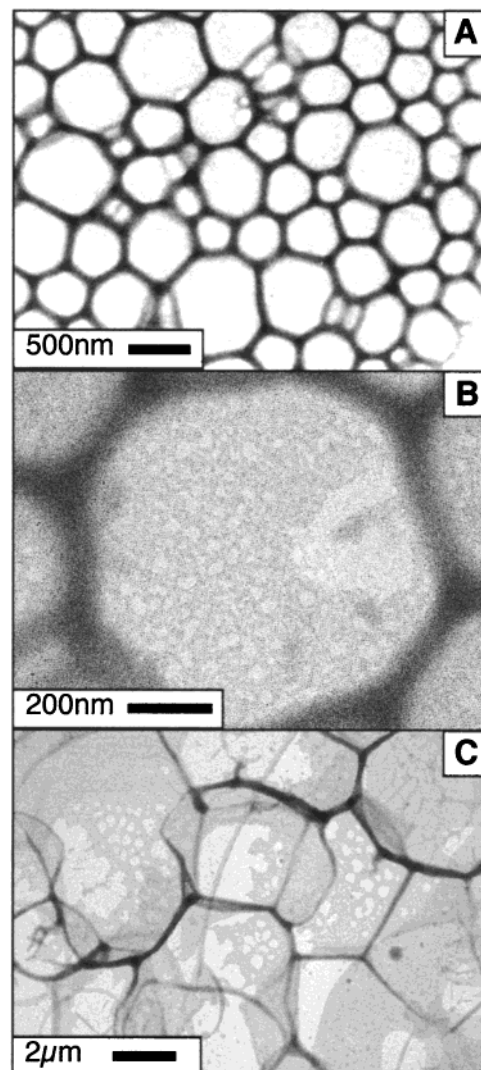


Figure 7. Hexagonal patterns obtained with “concentrated” solutions of silver (A and B) and more chaotic patterns (C). Coverage ratio is between 1 and 3.

corresponds to procedure II. The liquid containing nanocrystals undergoes a fingering instability at the wetting frontline during the droplet spreading. Figure 8 shows a progressive growth of fingering patterns with evaporation time. (It has been impossible to record the feature immediately after deposition.) An increase in the fingering periodicity from 120 to 200 μm is observed. At the final stage, when solvent is totally evaporated, fingering patterns are still homogeneous in shape and periodicity (Figure 8E). The final average distance between the fingers is $206 \pm 24 \mu\text{m}$. These instabilities are still observable, due to the remaining nanocrystals deposited on the support. Hence, the particle density profile prints the liquid flows and the instabilities during the evaporation. Similar fingering prints were observed by applying gravitational or centrifugal force or surface shear stress.³¹ Cazabat et al.³² reported another example of such an instability-driven flow, attributed to the Marangoni effect. In the latter case, a temperature gradient induces a surface tension gradient, driving the spreading process. In the present experiments, evaporation induces simultaneously a nanocrystal concentration and a temperature gradient. Both of these factors are expected to generate a surface tension gradient, driving instabilities and periodic patterns.

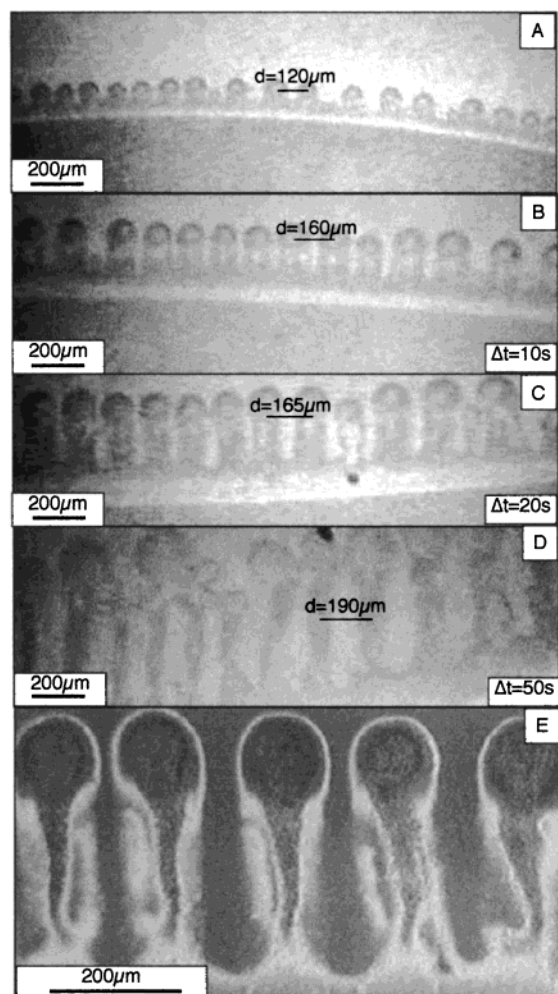


Figure 8. Fingering patterns obtained from a concentrated solution of silver particles dispersed in hexane, following procedure II. Coverage ratio is 5. Pictures are obtained at different times during the spreading of the droplet. (from A to D) and after evaporation of the solvent (E) (with an another sample).

6. Conclusion

From the data presented here, it appears that a fast evaporation process induces a large perturbation of the system in a nonequilibrium state. Consequently, the liquid film interface is modified and convection occurs. The nanocrystal density is also modulated in the interface plane with a similar periodicity, depending on the flow transport, interface modification, and evaporation. In any case, on decreasing the film height by evaporation, the long-wavelength Marangoni instabilities appear. Hence, film rupture locally occurs in the low particle density areas because it corresponds to the thinner areas of the film. Then, convective flow, close to the frontline front of this hole, further increases the nanocrystal density. This explains why single holes have anomalously high local nanocrystal densities. Furthermore, due to capillary forces, the film retraction, by a hole nucleation process, drags nanocrystals and further increases the local high-density areas.

Acknowledgment. Our special thanks to P. André, N. Pinna, and J. Legrand for providing us with copper, triangular cadmium sulfide, and cobalt nanocrystals, respectively, and Dr. V. Yaminsky for fruitful discussions.

Appendix 1: Nanocrystal Synthesis

Silver Nanocrystals²⁵. Colloidal silver particles were prepared by mixing two reverse micellar solutions having the same water-content $w = [\text{H}_2\text{O}]/[\text{AOT}] = 40$

Solution 1: $[\text{Ag}(\text{AOT})] = 0.06 \text{ M}$; $[\text{Na}(\text{AOT})] = 0.04 \text{ M}$;
 $[\text{H}_2\text{O}] = 0.2 \text{ M}$

Solution 2: $[\text{Na}(\text{AOT})] = 0.1 \text{ M}$, $[\text{N}_2\text{H}_4] = 0.14 \text{ M}$

After synthesis, particles are coated with dodecanthiol, extracted from the micellar solution and dispersed in hexane. The size distribution is reduced by a size-selection precipitation as described in ref 25.

Cobalt Nanocrystals. Cobalt nanocrystals are obtained by adding NaBH_4 to a micellar solution of $\text{Co}(\text{AOT})_2$ at $w = 40$. $[\text{Co}(\text{AOT})_2] = 0.1 \text{ M}$; $[\text{NaBH}_4] = 6.7 \times 10^{-2} \text{ M}$. The cobalt nanocrystal are then coated with lauric acid ($\text{C}_{12}\text{H}_{25}\text{COOH}$), extracted from micellar solution and dispersed in hexane.

Copper Nanocrystals^{26,27}. Colloidal copper nanocrystals are prepared by mixing the reverse micellar system with an aqueous solution of hydrazine. $[\text{Cu}(\text{AOT})_2] = 0.1 \text{ M}$; $[\text{N}_2\text{H}_4] = 0.3 \text{ M}$ ($w = 36$)

Ag_2S Nanocrystals³. Ag_2S nanocrystals are prepared by mixing a 0.1 M NaAOT reverse micellar solution containing AgAOT, with a sodium sulfide, Na_2S , aqueous solution. The AgAOT and Na_2S concentrations are $4 \times 10^{-4} \text{ M}$ and the water content is $w = 20$. After synthesis, particles are coated with dodecanthiol, extracted from the micellar solution and dispersed in heptane.

Triangular CdS Nanocrystals²⁸. CdS nanocrystals are formed by diffusing a mixture of H_2S and N_2 gas in a $\text{Cd}(\text{AOT})_2$ micellar solution. A coprecipitation reaction takes place between Cd^{2+} and S^{2-} ions with a molar fraction of 1/3. Particles are coated with dodecanthiol and extracted from the micellar solution. $[\text{Cd}(\text{AOT})_2] = 5 \times 10^{-2} \text{ M}$; $\text{H}_2\text{S}/\text{N}_2$ gas flow = $0.05 \text{ cm}^3 \text{ s}^{-1}$; $w = 30$.

Ferrite Nanocrystals²⁴. Ferrous dodecyl sulfate $[\text{Fe}(\text{DS})_2] = 1.3 \times 10^{-2} \text{ M}$ is solubilized in aqueous solution and kept at 28.5°C . Dimethylamine, $[(\text{CH}_3)_2\text{NH}_2\text{OH}] = 0.85 \text{ M}$, is added to the micellar solution with vigorous stirring for 2 h. The particles are coated with sodium citrate $[\text{Na}_3\text{C}_6\text{O}_7\text{H}_5] = 1.5 \times 10^{-2} \text{ M}$ and dispersed in aqueous solution or coated with lauric acid $[\text{C}_{12}\text{H}_{25}\text{COOH}] = 0.12 \text{ M}$ and dispersed in hexane.

References and Notes

- (1) Ohara, P. C.; Gelbart, W. M. *Langmuir* **1998**, *14*, 3418.
- (2) Kurrika, V.; Shafi, P. M.; Felner, I.; Mastai, Y.; Gedanken, A. *J. Phys. Chem. B* **1999**, *103*, 3358.
- (3) Motte, L.; Billoudet, F.; Pileni, M. P. *J. Phys. Chem.* **1995**, *99*, 16425.
- (4) Motte, L.; Lacaze, E.; Maillard, M.; Pileni, M. P. *Langmuir* **2000**, *16*, 3803.
- (5) Taleb, A.; Petit, C.; Pileni, M. P. *J. Phys. Chem. B* **1998**, *102*, 2214.
- (6) Taleb, A.; Russier, V.; Courty, A.; Pileni, M. P. *Phys. Rev. B* **1999**, *59*, 13350.
- (7) Petit, C.; Taleb, A.; Pileni, M. P. *Adv. Mater.* **1998**, *10*, 259.
- (8) Russier, V.; Petit, C.; Legrand, J.; Pileni, M. P. *Phys. Rev. B* **2000**, *62*, 3910.
- (9) Ngo, A. T.; Pileni, M. P. *Adv. Mater.* **2000**, *12*, 276.
- (10) Oron, A.; Davis, S. H.; Bankoff, S. G. *Rev. Mod. Phys.* **1997**, *69*, 931.
- (11) Yaminsky, V. V.; Thuresson, K.; Ninham, B. W. *Langmuir* **1999**, *15*, 3683.
- (12) Bénard, H. *Rev. Gen. Sci. Pures Appl.* **1900**, *11*, 1261.
- (13) Block, M. *Nature* **1956**, *178*, 650.
- (14) Pearson, J. R. A. *J. Fluid Mech.* **1958**, *4*, 489.

- (15) Koschmieder, E. L. *J. Fluid Mech.* **1967**, *30*, 9.
- (16) Ondaçuhu, T.; Millan-Rodriguez, J.; Mancini, H. L.; Garcimartin, A.; and Perez-Garcia, C. *Phys. Rev. E* **1993**, *48*, 1051.
- (17) Fanton, X.; Cazabat, A. M. *Langmuir* **1998**, *14*, 2554.
- (18) Lord Rayleigh, *Philos. Mag.* **1916**, *32*, 529.
- (19) VanHook, S. J.; Shatz, M. F.; McCornick, W. D.; Swift, J. B.; Swinney, H. L. *Phys. Rev. Lett.* **1995**, *75* (24), 4397.
- (20) Brochard-Wyart, F.; diMeglio, J. M.; Quéré, D.; deGennes, P. G. *Langmuir* **1991**, *7*, 335.
- (21) Petit, C.; Lixon, P.; Pileni, M. P. *J. Phys. Chem.* **1990**, *94*, 1598.
- (22) Moumen, N.; Veillet, P.; Pileni, M. P. *J. Magn. Magn. Mater.* **1995**, *67*, 149.
- (23) Pileni, M. P. *Langmuir* **1997**, *13*, 3266.
- (24) Ngo, A. T. Bonville, P.; Pileni, M. P. *Eur. Phys. J. B* **1999**, *9*, 583.
- (25) Taleb, A.; Petit, C.; Pileni, M. P. *Chem Mater.* **1997**, *9*, 950.
- (26) Tanori, J.; Pileni, M. P. *Langmuir* **1997**, *13*, 639.
- (27) Pileni, M. P.; Ninham, B. W.; Gulik-Krzywicki, T.; Tanori, J.; Lisiecki, I.; Filankembo, A. *Adv. Mater.* **1999**, *11*, 1358.
- (28) Pinna, N.; Weiss, K.; Urban, J.; Pileni, M. P. *Advanced Materials*, in press.
- (29) Riddick, J. A.; Bunger, W. B.; Sakano, T. K. *Organic solvents, Physical properties and Methods of Purification*. In *Techniques of Chemistry*; J. Wiley Ed.: New York, Chichester, Brisbane, 1986.
- (30) Manneville, P. *Dissipative structures and weak turbulence*. In *Perspectives in physics*. Academic Press: Boston, 1990.
- (31) Huppert, H. E. *Nature* **1982**, *300*, 427.
- (32) Cazabat, A. M.; Heslot, F.; Troian, S. M.; Carles, P. *Nature* **1990**, *346*, 824.